

Small fraction of marine cloud condensation nuclei made up of sea spray aerosol

P. K. Quinn^{1,2*}, D. J. Coffman¹, J. E. Johnson^{1,2}, L. M. Upchurch^{1,2} and T. S. Bates^{1,2}

Sea spray aerosols impact Earth's radiation balance by directly scattering solar radiation. They also act as cloud condensation nuclei, thereby altering cloud properties including reflectivity, lifetime and extent. The influence of sea spray aerosol on cloud properties is thought to be particularly strong over remote ocean regions devoid of continental particles. Yet the contribution of sea spray aerosol to the population of cloud condensation nuclei in the marine boundary layer remains poorly understood. Here, using a lognormal-mode-fitting procedure, we isolate sea spray aerosols from measurements of particle size and abundance over the Pacific, Southern, Arctic and Atlantic oceans to determine the contribution of sea spray aerosol to the population of cloud condensation nuclei in the marine boundary layer. On a global basis, with the exception of the high southern latitudes, sea spray aerosol makes a contribution of less than 30% to the cloud condensation nuclei population for air that is supersaturated at 0.1 to 1.0%—the supersaturation range typical of marine boundary layer clouds. Instead, the cloud condensation nuclei population between 70° S and 80° N is composed primarily of non-sea-salt sulfate aerosols, due to large-scale meteorological features that result in entrainment of particles from the free troposphere.

The wind-driven production of sea spray aerosol (SSA) is one of the largest global sources of primary atmospheric aerosol particles on a mass concentration basis¹. Measurements in the marine boundary layer (MBL) reveal that the primary inorganic sea salt component of SSA dominates the marine aerosol mass size distribution, especially for diameters larger than about 500 nm (geometric mean diameter, D_g , at 80% relative humidity (RH))^{2,3}. As a result, SSA is known to be the dominant contributor to aerosol light scattering in the MBL^{4–6}. Model estimates of the cooling at Earth's surface due to scattering by SSA range from 0.08 to 6 W m⁻² (ref. 7). The wide range of these estimates results, in large part, from uncertainty in the SSA source function⁸. The contribution of SSA to the MBL cloud condensation nuclei (CCN) population and its relative importance in indirect effects over ocean regions is even more uncertain⁹.

The MBL number size distribution consists of a varying and complex mixture of primary SSA (including organics and inorganic sea salt), secondary non-sea-salt (nss) SO₄²⁻ resulting from the oxidation of ocean-derived dimethyl sulfide (DMS), secondary ocean-derived organics, and aerosols and precursor gases emitted from continental sources (fossil fuel combustion, biomass burning, dust and biogenic emissions). Recent studies have focused on the organic component of SSA as a potentially major source of MBL particle number^{10–14}. Isolating and quantifying the SSA fraction of the total MBL CCN population is challenging. The few reported direct chemical measurements of SSA number concentrations have employed either detection of emissions from thermally excited sodium atoms^{15,16} or transmission electron microscopy with energy-dispersive X-ray analysis^{17,18}. Indirect methods, based on aerosol volatility, have also been used^{19,20}. The use of all of these methods has been limited, however.

Another approach for determining the SSA fraction of the total MBL number population using a lognormal-mode-fitting procedure that isolates the SSA mode from the total aerosol number

size distribution has recently been reported²¹. The resulting mode is similar in shape to a canonical SSA size distribution constructed from number size distributions measured in the MBL over the period from 1951 to 2001²² and generated from simulated breaking waves in a wave channel²³. The broad nature of the mode, with a D_g between 0.16 and 0.3 μm (dry RH) and a geometric standard deviation (σ_g) of 3, indicates that it encompasses a broad range of diameters that may result from different wind-driven production mechanisms^{24,25}. To date, this approach has been applied to data collected during a cruise off the coast of California in 2011²¹. It was found that SSA typically made up less than 15% of the MBL particle number concentration and 5 to 63% of the CCN at supersaturations less than 0.3%.

To extend these results to the world's oceans, we have applied a similar lognormal-mode-fitting procedure to MBL aerosol number size distributions measured during seven research cruises in the Pacific, Southern, Arctic and North Atlantic oceans between 1993 and 2015 (Fig. 1 and Supplementary Table 1). Cruises conducted during this period that were strongly influenced by continental aerosols (aerosol light absorption coefficient > 0.80 Mm⁻¹ and radon concentration > 540 mBq m⁻³) were omitted. As a result, this analysis provides an upper bound on the contribution of SSA to the MBL CCN population. Measured mass concentrations of Na⁺, a proxy for sea salt, were used to confirm the ocean source of the lognormally fitted SSA mode (Methods). Presented here are observed contributions of SSA to the MBL particle number and CCN populations for four different oceans over latitudes ranging from 70° S to 80° N. These results do not include potentially significant impacts of giant CCN ($D_g > 10 \mu\text{m}$) on cloud optical properties and precipitation²⁶ due to the size range of particles considered.

Number fraction of sea spray aerosol particles

Three modes resulted from lognormal fitting of the measured number size distributions including Aitken and accumulation

¹NOAA Pacific Marine Environmental Laboratory, Seattle, Washington 98115, USA. ²University of Washington, Joint Institute for the Study of the Atmosphere and Ocean, Seattle, Washington 98195, USA. *e-mail: patricia.k.quinn@noaa.gov

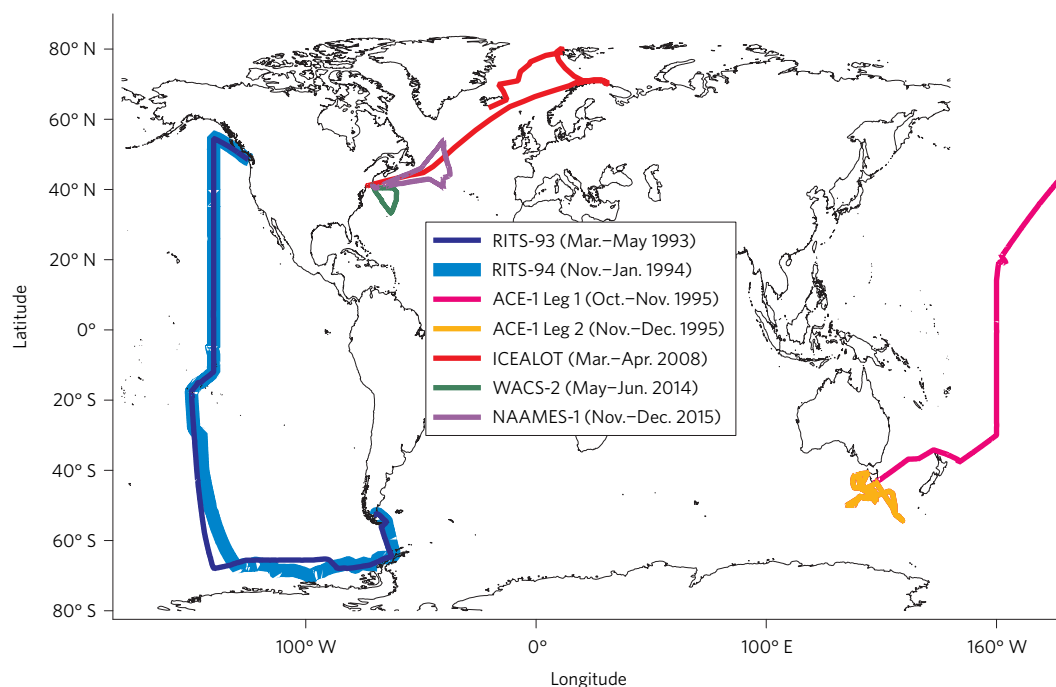


Figure 1 | Cruise tracks and dates of the seven experiments included in this analysis. These cruises were included in the analysis to obtain a broad representation of the world's oceans while minimizing continental influence. Data from all cruises can be found at <http://saga.pmel.noaa.gov/data>.

modes with values of D_g ranging from 0.02 to 0.08 μm and 0.10 to 0.23 μm , respectively, and a SSA mode with values of D_g ranging from 0.17 to 0.45 μm ($\sigma_g = 2.2$ to 2.8) (Fig. 2a and Supplementary Table 2). Differences in sampling humidities and size distribution instrumentation contributed to the variability between cruises (Methods). In addition, volume modes were derived from the number modes (Fig. 2b).

For an independent check on the existence of a SSA mode within the measured number size distributions, mass concentrations of sub-10 μm Na^+ from ion chromatography analysis of impactor samples were compared with the number of particles within the corresponding averaged size distribution with diameters greater than 0.5 μm , $N_{(D_g > 0.5 \mu\text{m})}$. Restricting the summed number concentration to this size range omits all of the Aitken mode and most of the accumulation mode, thereby isolating the SSA mode (Fig. 2a). A linear regression between sub-10 μm Na^+ and $N_{(D_g > 0.5 \mu\text{m})}$ concentrations resulted in coefficients of determination, r^2 , ranging from 0.51 to 0.89 for the seven experiments (Supplementary Fig. 1), indicating that particles in the $D_g > 0.5 \mu\text{m}$ size range were composed primarily of sea salt, confirming the existence of a SSA mode.

To confirm that the fitting procedure successfully isolated the SSA mode, sub-10 μm Na^+ mass concentrations were compared to total number and volume concentrations within the lognormally fitted SSA mode. The resulting r^2 values ranged from 0.21 to 0.89 and 0.48 to 0.94 for the number and volume modes, respectively, for the seven cruises (Supplementary Fig. 2 and Supplementary Table 3), indicating that the fitting procedure was able to isolate the SSA mode. To identify the composition of the Aitken and accumulation modes, the number and volume concentration in each were compared to mass concentrations of sub-0.18 μm and sub-1 μm nss SO_4^{2-} from ion chromatography analysis and organic carbon (OC) from thermal-optical analysis of impactor samples. Accumulation-mode number and volume concentrations were moderately to strongly correlated with nss SO_4^{2-} ($r^2 = 0.20$ to 0.92) for all cruises, while weak to moderate correlations were found for OC (r^2 of 0.03 to 0.54) (Supplementary Fig. 2 and Supplementary Table 3). On the basis of these results, nss SO_4^{2-} dominated the accumulation-mode size range although OC also contributed. Few

significant correlations were found between Aitken-mode number or volume concentrations and sub-0.18 μm Na^+ , nss SO_4^{2-} or OC mass concentrations (Supplementary Tables 3 and 4), probably due to the low mass concentrations in this size range leading to larger sampling and fitting uncertainties (Methods; Supplementary Fig. 3). Measured average mass concentrations of Na^+ , nss SO_4^{2-} and OC are given in Supplementary Table 4.

The number fraction of SSA was calculated from the total number concentration in the lognormally fitted SSA mode divided by the sum of the number concentration in the Aitken, accumulation and SSA fitted modes (Fig. 3a). Values from the seven experiments were then combined into 10° latitude bins (Fig. 3b). Supplementary Table 5 lists the binned modal number fractions and the seasonal coverage for each bin. Across all latitude bins, from 70° S to 80° N, the SSA mode made up 15% or less of the total particle number concentration. Averaging all data into 2 m s^{-1} wind speed bins indicates that SSA number concentration and fraction increase with wind speed (Fig. 3c), with the number fraction being less than 25% for wind speeds up to 20 m s^{-1} .

The Aitken mode dominated the particle number concentration between 70° S and 20° S with average number fractions ranging from 48 to 72% (Fig. 3b and Supplementary Table 5). Data within this latitude band were obtained from cruises that took place in the Pacific and Southern oceans during austral autumn, summer and spring. Similar large-scale meteorological features were present during all of these cruises. At latitudes south of ~40° S, low-pressure systems moved through the sampling region every few days^{27–29}. Air mass back trajectories indicated that entrainment of air from above the MBL height of about 1,000 m was associated with the frontal passages^{28,29}. During one cruise, ACE-1 Leg 1, aircraft observations revealed layers of high concentrations (2,000 to 4,000 cm^{-3}) of ultrafine particles (D_g of 0.012 μm) associated with cloud outflows³⁰. Modelling studies³¹ and observations^{32,33} have shown that conditions in cloud outflow regions in the free troposphere are favourable for new particle production via homogeneous nucleation of precursor gases^{31,32,34,35}. Hence, air entrained from the free troposphere often contains Aitken-mode particles. Once in the MBL, Aitken-mode particles grow to the

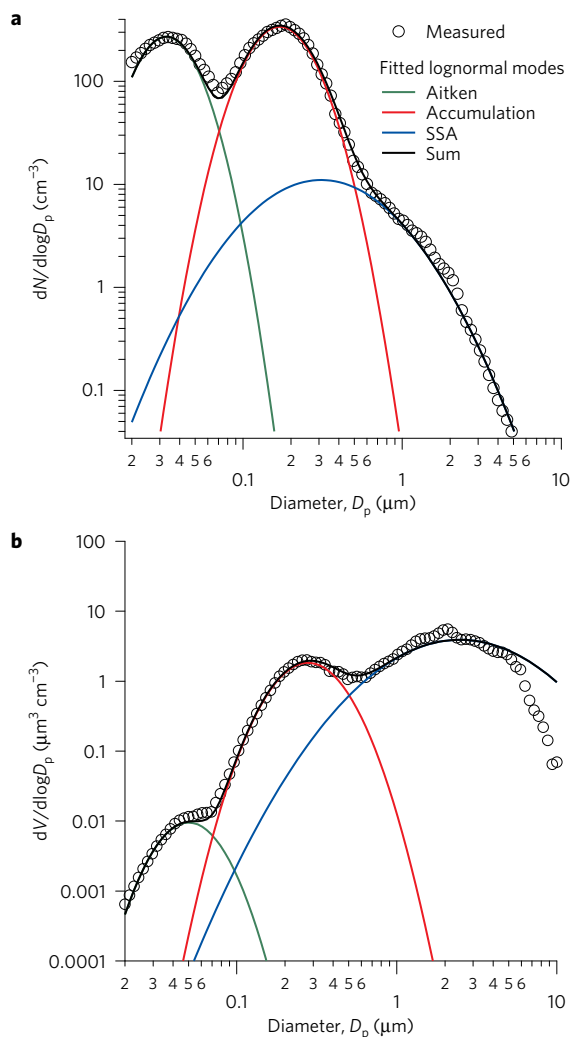


Figure 2 | Fitted lognormal modes based on number size distributions measured during ICEALOT. a, b, Size distributions were averaged over a 10-hour period (the length of an impactor sample) and fitted for number (a) and volume (b). The size distributions were measured on 4 April 2008 while the ship was near 68.45° N and 9.0° W, northeast of Iceland. The average wind speed over the period was $12.4 \pm 1.8 \text{ m s}^{-1}$.

accumulation-mode size range through vapour condensation and accumulation of mass during cloud processing in stratus and stratocumulus clouds^{36,37}. The calculated trajectories also showed that the frequent frontal passages limited the residence time of MBL Aitken-mode particles to one to three days, which prevented growth to the accumulation-mode size range before removal through wet deposition^{27,29}. As a result, the average number fraction of Aitken-mode particles was larger than that of accumulation-mode particles. This pattern persisted in the southern mid-latitudes ($\sim 40^\circ \text{ S}$ to 20° S) due to the occurrence of strong high-pressure systems and associated subsidence of air from the free troposphere.

Aitken- and accumulation-mode number fractions were comparable in the tropics of the western and central Pacific (Fig. 3a, b and Supplementary Table 5). Stable air masses and persistent trade wind flow resulted in longer aerosol residence times (5 days or more on the basis of calculated back trajectories), which allowed for growth of the Aitken-mode to accumulation-mode sizes^{28,29}. Data from the 20° N to 60° N latitude band were obtained from cruises that took place in the Pacific and Atlantic oceans in spring and autumn. Meteorological features for all cruises in this latitude band included periods of stable cloud-topped

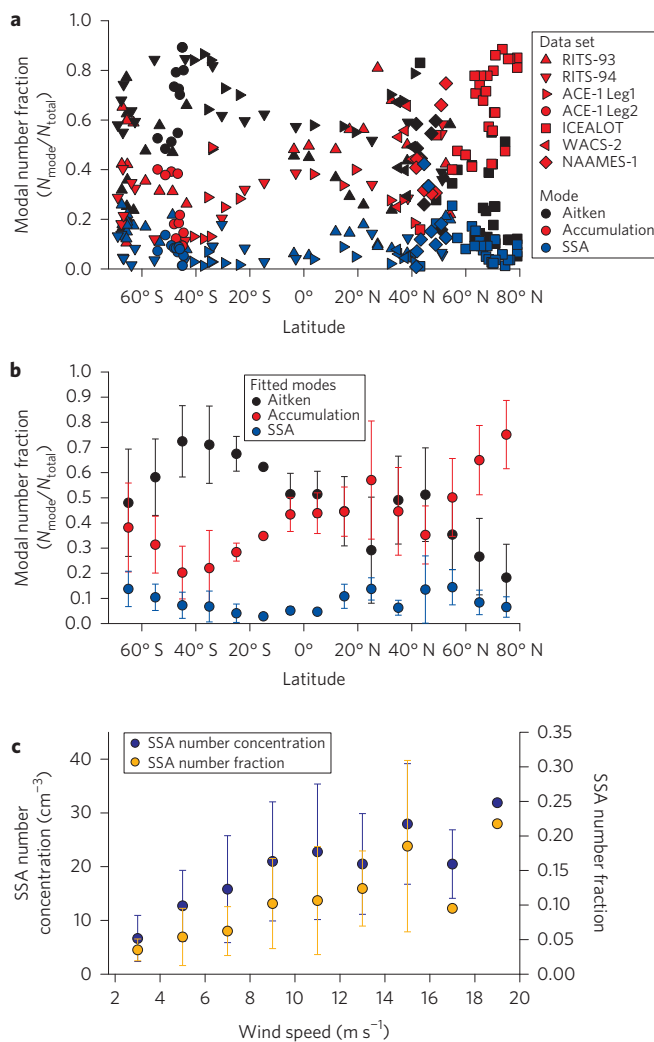


Figure 3 | Number fraction of the lognormally fitted Aitken, accumulation and SSA modes. a–c, Data are shown as all number size distributions used in the analysis averaged over the corresponding impactor samples (a), average and standard deviation (1σ) of the latitudinally binned data (b), and average and standard deviation (1σ) of the SSA number concentration and number fraction binned by 2 m s^{-1} wind speeds (c).

MBLs disrupted by frontal passages with associated entrainment, resulting in variable Aitken- and accumulation-mode number fractions (29 to 51% and 35 to 57%, respectively). Continental sources may also have contributed to variability in the calculated number fractions.

The accumulation mode dominated the particle number concentration in the 60° N to 80° N latitude band with number fractions of 65% (60° N to 70° N) and 75% (70° N to 80° N) (Fig. 3b and Supplementary Table 5). These data were collected in the spring, which is Arctic haze season. Radiosonde data showed the presence of strong temperature inversions that minimized vertical mixing between the free troposphere and the boundary layer while calculated back trajectories indicated the transport of air masses from Europe into the sampling region and MBL aerosol residence times longer than 5 days³⁸. The stable, stratified atmosphere with little wet deposition coupled with the transport of air masses from southern source regions led to a large accumulation-mode number concentration. The same latitude bands in the summer are likely to have a relatively larger Aitken-mode number concentration due to less efficient transport, increased wet removal, and local biogenic secondary aerosol production^{39,40}.

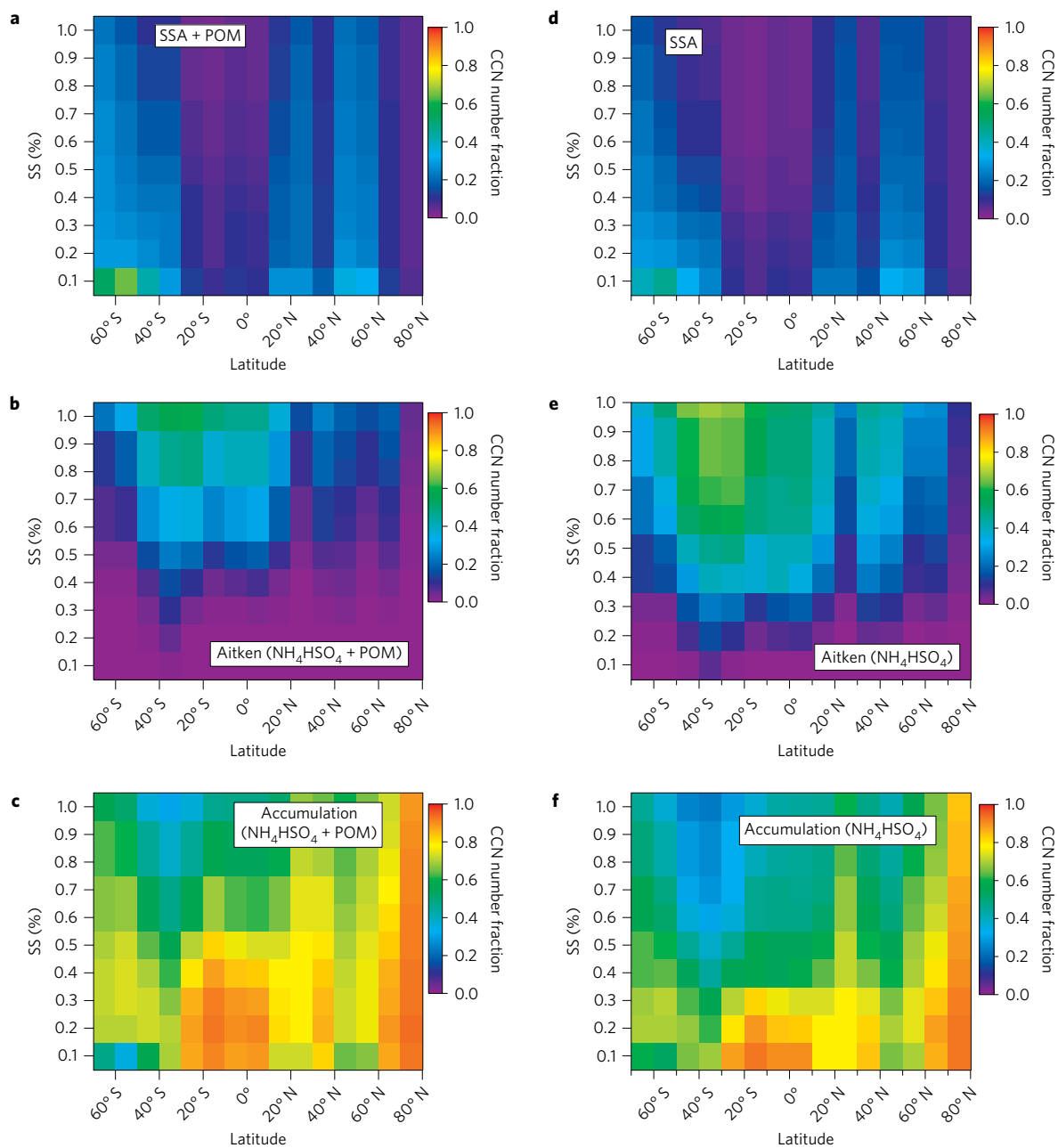


Figure 4 | Calculated CCN modal number fraction as a function of supersaturation and latitude. a–f, Data are based on combined, latitudinally binned data from RITS-93, RITS-94, ACE-1 Legs 1 and 2, ICEALOT, WACS-2 and NAAMES-1 for the SSA mode with a composition of sea salt and POM (a), Aitken mode for a composition of nss SO_4^{2-} (as NH_4HSO_4) and POM (b), accumulation mode for a composition of nss SO_4^{2-} (as NH_4HSO_4) and POM (c), SSA mode as pure SSA (d), Aitken mode as pure nss SO_4^{2-} (as NH_4HSO_4) (e) and accumulation mode as pure nss SO_4^{2-} (as NH_4HSO_4) (f).

Sea spray aerosol cloud condensation nuclei

Modal number size distributions and measured chemical composition were used to calculate modal CCN number concentrations. Two extremes of chemical composition were used to calculate the range of CCN number concentrations for each mode. In the first case, each mode was assumed to be completely water soluble with the Aitken and accumulation modes composed of nss SO_4^{2-} (as NH_4HSO_4) and the SSA mode composed of inorganic sea salt. With completely soluble Aitken and accumulation modes, this case provides a lower bound of the SSA CCN number fraction. In the second case, an insoluble organic component was added to each mode to provide an upper bound for the SSA CCN number fraction. Supplementary Fig. 7 shows the sensitivity of the CCN modal number fraction for the range of observed particulate organic matter (POM) mass

fractions. The critical diameter, D_c , where a particle is large enough and contains sufficient soluble material to become a CCN, was calculated using Köhler theory⁴¹ over supersaturations ranging from 0.1 to 1.0% for the two cases (Methods). This range encompasses previously reported measured effective supersaturations of MBL clouds^{42–46}. Modal CCN concentrations were derived by summing the number of all particles in the fitted mode with diameters greater than D_c .

The accuracy of modelled CCN concentrations was assessed by comparing the sum of CCN calculated to be in the three modes with CCN concentrations measured during the ICEALOT cruise, which had the most complete CCN data set (Methods). Including insoluble POM improved the agreement between measured and modelled values so that the difference was less than 5% for

supersaturations ranging from 0.3 to 0.5% (Supplementary Fig. 8). At 0.2% supersaturation, the model underestimated the total CCN concentration by $20 \pm 10\%$. This degree of agreement between modelled and measured CCN concentrations lends confidence in the calculated modal CCN concentrations. CCN modal number fractions for both cases of chemical composition are shown in Fig. 4 with underlying data in Supplementary Tables 6–11. The discussion below focuses on the composition case that includes insoluble POM.

The largest SSA CCN number fractions, up to 65%, were observed in the high southern latitudes (40° S to 70° S) at low supersaturation (0.1%) (Fig. 4a). A second region of enhanced SSA CCN number fractions (up to 35% at 0.1% supersaturation) occurred between 40° N and 60° N. The large diameter and high hygroscopicity of SSA compared with the Aitken mode, which either dominated or made significant contributions to the particle number concentration in these latitude bands (Fig. 3a), led to the enhanced SSA CCN number fractions. For all other regions and supersaturations, the SSA mode made up less than 30% of the total CCN, with even lower number fractions (<20%) for the majority of latitude bins and supersaturations considered (Fig. 4a and Supplementary Table 7).

The largest Aitken-mode CCN number fractions occurred in the southern hemisphere and the tropics at supersaturations greater than 0.5% (Fig. 4b and Supplementary Table 9). The Aitken mode dominated the number concentration in these regions due to entrainment of newly formed particles from the upper troposphere. Due to the small diameter of the Aitken mode relative to the accumulation and SSA modes, Aitken-mode CCN number fractions were significant only at higher supersaturations with values ranging from 3% to 24% at 0.5% supersaturation and from 22 to 58% at 1.0% supersaturation. The large Aitken-mode organic content in the $\text{NH}_4\text{HSO}_4 + \text{POM}$ case in the North Atlantic (Supplementary Fig. 4) also led to lower CCN number fractions, even at higher supersaturations.

Apart from the high southern latitudes at 0.1% supersaturation and the southern mid-latitudes at high supersaturations (<0.5%), the accumulation mode dominated the MBL CCN number population (Fig. 4c and Supplementary Table 11). This result is due to its larger number concentration relative to the SSA mode and its larger diameter and lower POM mass fraction compared with the Aitken mode. The highest accumulation-mode CCN number fractions occurred in regions with the longest MBL residence times (tropics and Arctic), which allowed for the growth of Aitken-mode particles into the accumulation-mode size range before removal through deposition. The results for the Arctic from this analysis are skewed toward the Arctic haze season. Summertime measurements would probably reveal higher Aitken-mode CCN number fractions at high supersaturations due to biogenic secondary aerosol production^{39,40}.

Marine boundary layer cloud condensation nuclei budget

These results indicate that persistent, large-scale meteorological features, which result in entrainment of particles from the free troposphere into the MBL and regionally varying MBL aerosol residence times, drive the MBL CCN budget. Aitken-mode particles make up a large fraction of the CCN in the Southern Hemisphere at high supersaturations (>0.5%) due to entrainment from the free troposphere and short residence times that limit the growth of these particles into the accumulation-mode size range. Being larger in diameter and more hygroscopic than Aitken-mode particles, SSA, including both the inorganic and organic fractions, dominates the CCN population in the high latitudes of the Southern Hemisphere region at low supersaturations. For all other regions and supersaturations, accumulation-mode nss SO_4^{2-} dominates the MBL CCN population. Open questions remain, however, on the source of MBL nss SO_4^{2-} with possibilities including DMS oxidation to SO_2 in the MBL that leads to particle growth⁴⁷, DMS oxidation in the free troposphere followed by entrainment to the MBL that leads to increased

particle number concentration³¹, and transport of anthropogenic emissions in either the MBL or free troposphere. Models equipped with accurate parameterizations of multi-phase DMS chemistry⁴⁸ and validated with empirical constraints, such as those presented here, will provide some answers. Measurements that provide additional seasonal and geographical coverage of MBL particle number size distributions and chemical composition as well as measurements able to differentiate between anthropogenic and biogenic sulfate, such as isotopic analysis^{49,50}, will provide additional information. Finally, SSA as ice nuclei⁵¹ and giant CCN²⁶ may have significant impacts on MBL cloud properties. Studies able to assess these impacts will help to further elucidate the climate impacts of SSA.

Methods

Methods, including statements of data availability and any associated accession codes and references, are available in the [online version of this paper](#).

Received 27 January 2017; accepted 7 July 2017;
published online 14 August 2017

References

- Warneck, P. *Chemistry of the Natural Atmosphere* (San Diego Academic, 1988).
- McInnes, L. M., Quinn, P. K., Covert, D. S. & Anderson, T. L. Gravimetric analysis, ionic composition, and associated water mass of the marine aerosol. *Atmos. Environ.* **30**, 869–884 (1996).
- Quinn, P. K. & Coffman, D. J. Local closure during ACE 1: aerosol mass concentration and scattering and backscattering coefficients. *J. Geophys. Res.* **103**, 16575–16596 (1998).
- Quinn, P. K. & Coffman, D. J. Comment on “Contribution of different aerosol species to the global aerosol extinction optical thickness: estimates from model results” by Tegen *et al.* *J. Geophys. Res.* **104**, 4241–4248 (1999).
- Jacobson, M. Z. Global direct radiative forcing due to multicomponent anthropogenic and natural aerosols. *J. Geophys. Res.* **106**, 1551–1568 (2001).
- Takemura, T. *et al.* Single-scattering albedo and radiative forcing of various aerosol species with a global three-dimensional model. *J. Clim.* **15**, 333–352 (2002).
- de Leeuw, G. *et al.* Production flux of sea spray aerosol. *Rev. Geophys.* **49**, RG2001 (2011).
- Ovadnevaite, J. *et al.* A sea spray aerosol flux parameterization encapsulating wave state. *Atmos. Chem. Phys.* **14**, 1837–1852 (2014).
- Tsigaridis, K., Koch, D. & Menon, S. Uncertainties and importance of sea spray composition on aerosol direct and indirect effects. *J. Geophys. Res.* **118**, 220–235 (2013).
- O’Dowd, C. D. *et al.* Biogenically driven organic contribution to marine aerosol. *Nature* **431**, 676–680 (2004).
- Leck, C. & Bigg, E. K. Biogenic particles in the surface microlayer and overlying atmosphere in the central Arctic Ocean during summer. *Tellus B* **57**, 305–316 (2005).
- Keene, W. C. *et al.* Chemical and physical characteristics of nascent aerosols produced by bursting bubbles at a model air-sea interface. *J. Geophys. Res.* **112**, D21202 (2007).
- Facchini, M. C. *et al.* Important source of marine secondary organic aerosol from biogenic amines. *Environ. Sci. Technol.* **42**, 9116–9121 (2008).
- Quinn, P. K. & Bates, T. S. The case against climate regulation via oceanic phytoplankton sulfur emissions. *Nat. Geosci.* **4**, 51–56 (2011).
- Campuzano-Jost, P. *et al.* Near real-time measurement of sea-salt aerosol during the SEAS Campaign: comparison of emission-based sodium detection with an aerosol volatility technique. *J. Atmos. Oceanic Tech.* **20**, 1421–1430 (2003).
- Hobbs, P. V. Simultaneous airborne measurements of cloud condensation nuclei and sodium-containing particles over the ocean. *Q. J. R. Meteorol. Soc.* **97**, 263–271 (1971).
- McInnes, L. M., Covert, D. S. & Baker, B. The number of sea-salt, sulfate, and carbonaceous particles in the marine atmosphere: EM measurements consistent with the ambient size distribution. *Tellus B* **49**, 300–313 (1997).
- Murphy, D. M. *et al.* Influence of sea-salt on aerosol radiative properties in the Southern Ocean marine boundary layer. *Nature* **392**, 62–65 (1998).
- Dinger, J. E., Howell, H. B. & Wojciechowski, T. A. On the source and composition of cloud nuclei in a subsident air mass over the North Atlantic. *J. Atmos. Sci.* **27**, 791–797 (1970).
- O’Dowd, C. D., Smith, M. H. & Jennings, S. G. Submicron particle, radon, and soot carbon characteristics over the northeast Atlantic. *J. Geophys. Res.* **98**, 1123–1135 (2003).

21. Modini, R. L. *et al.* Primary marine aerosol-cloud interactions off the coast of California. *J. Geophys. Res.* **120**, 4282–4303 (2015).
22. Lewis, E. R. & Schwartz, S. E. *Sea Salt Aerosol Production: Mechanisms, Methods, Measurements, and Models - A Critical Review* (American Geophysical Union, 2004).
23. Prather, K. A. *et al.* Bringing the ocean into the laboratory to probe the chemical complexity of sea spray aerosol. *Proc. Natl Acad. Sci. USA* **110**, 7550–7555 (2013).
24. Spiel, D. E. On the births of film drops from bubbles bursting on seawater surfaces. *J. Geophys. Res.* **103**, 24907–24918 (1998).
25. Bikerman, J. J. *Foams* (Springer, 1973).
26. Feingold, G., Cotton, W. R., Kreidenweis, S. M. & Davis, J. T. The impact of giant cloud condensation nuclei on drizzle formation in stratocumulus: implications for cloud radiative properties. *J. Atmos. Sci.* **56**, 4100–4117 (1998).
27. Bates, T. S. *et al.* Processes controlling the distribution of aerosol particles in the lower marine boundary layer during the First Aerosol Characterization Experiment (ACE 1). *J. Geophys. Res.* **103**, 16369–16383 (1998).
28. Covert, D. S., Kapustin, V. N., Bates, T. S. & Quinn, P. K. Physical properties of marine boundary layer aerosol particles of the mid-Pacific in relation to sources and meteorological transport. *J. Geophys. Res.* **101**, 6919–6930 (1996).
29. Quinn, P. K., Kapustin, V. N., Bates, T. S. & Covert, D. S. Chemical and optical properties of marine boundary layer aerosol particles of the mid-Pacific in relation to sources and meteorological transport. *J. Geophys. Res.* **101**, 6931–6951 (1996).
30. Clarke, A. *et al.* Particle production in the remote marine atmosphere: cloud outflow and subsidence during ACE-1. *J. Geophys. Res.* **103**, 16397–16409 (1998).
31. Raes, F. Entrainment of free-tropospheric aerosol as a regulating mechanism for cloud condensation nuclei in the remote marine boundary layer. *J. Geophys. Res.* **100**, 2893–2903 (1995).
32. Clarke, A. Atmospheric nuclei in the Pacific midtroposphere: their nature, concentration, and evolution. *J. Geophys. Res.* **98**, 20633–20647 (1993).
33. Bigg, E. K., Leck, C. & Nilsson, E. D. Sudden changes in Arctic atmosphere aerosol concentrations during summer and autumn. *Tellus B* **48**, 254–271 (1996).
34. Gras, J. L. Postfrontal nanoparticles at Cape Grim: impact on cloud nuclei concentrations. *Environ. Chem.* **6**, 515–523 (2009).
35. Gras, J. L., Jimi, S. I., Siems, S. T. & Krummel, P. B. Postfrontal nanoparticles at Cape Grim: observations. *Environ. Chem.* **6**, 508–514 (2009).
36. Hegg, D. A., Covert, D. S. & Kapustin, V. N. Modeling a case of particle nucleation in the marine boundary layer. *J. Geophys. Res.* **97**, 9851–9857 (1992).
37. Hoppel, W. A., Frick, G. M., Fitzgerald, J. W. & Larson, R. E. Marine boundary layer measurements of new particle formation and the effect which nonprecipitating clouds have on the aerosol size distribution. *J. Geophys. Res.* **99**, 14443–14459 (1994).
38. Frossard, A. A. *et al.* Springtime Arctic haze contributions of submicron organic particles from European and Asian combustion sources. *J. Geophys. Res.* **116**, D05205 (2011).
39. Tunved, P., Strom, J. & Krejci, R. Arctic aerosol life cycle: linking aerosol size distributions observed between 2000 and 2010 with air mass transport and precipitation at Zeppelin station, Ny-Ålesund, Svalbard. *Atmos. Chem. Phys.* **13**, 3643–3660 (2013).
40. Leaitch, W. R. *et al.* Dimethyl sulfide control of the clean summertime Arctic aerosol and cloud. *Elem. Sci. Anth.* **1**, 17 (2013).
41. Fitzgerald, J. W. Measurement of the relationship between the dry size and critical supersaturation of natural aerosol particles. *J. Appl. Meteorol.* **14**, 1044–1049 (1975).
42. Hoppel, W. A., Frick, G. M. & Fitzgerald, J. W. Deducing droplet concentration and supersaturation in marine boundary layer clouds from surface aerosol measurements. *J. Geophys. Res.* **101**, 26553–26565 (1996).
43. Leaitch, W. R. *et al.* Physical and chemical observations in marine stratus during the 1993 North Atlantic Regional Experiment: factors controlling cloud droplet number concentrations. *J. Geophys. Res.* **101**, 29123–29135 (1996).
44. Hudson, J. G. *et al.* Cloud condensation nuclei and ship tracks. *J. Atmos. Sci.* **57**, 2696–2706 (2000).
45. Roberts, G., Mauger, G., Hadley, O. & Ramanathan, V. North American and Asian aerosols over the eastern Pacific Ocean and their role in regulating cloud condensation nuclei. *J. Geophys. Res.* **111**, D13205 (2006).
46. Hudson, J. G., Noble, S. & Jha, V. Stratus cloud supersaturations. *Geophys. Res. Lett.* **37**, L21813 (2010).
47. Covert, D. S., Kapustin, V. N., Quinn, P. K. & Bates, T. S. New particle formation in the marine boundary layer. *J. Geophys. Res.* **97**, 20581–20589 (1992).
48. Hoffmann, E. H. *et al.* An advanced modeling study on the impacts and atmospheric implications of multi-phase dimethyl sulfide chemistry. *Proc. Natl Acad. Sci. USA* **113**, 11776–11781 (2016).
49. Calhoun, J. A., Bates, T. S. & Charlson, R. J. Sulfur isotope measurements of submicrometer sulfate aerosol particles over the Pacific Ocean. *Geophys. Res. Lett.* **18**, 1877–1880 (1991).
50. Norman, A. *et al.* Sources of aerosol sulphate at Alert: apportionment using stable isotopes. *J. Geophys. Res.* **104**, 11619–11631 (1999).
51. Burrows, S. M., Hoose, C., Poschl, U. & Lawrence, M. G. Ice nuclei in marine air: biogenic particles or dust? *Atmos. Chem. Phys.* **13**, 245–267 (2013).

Acknowledgements

This work was supported in part by the NOAA Climate Program Office. We thank the captain and crew of all of the NOAA and UNOLS vessels that contributed to this work. This is PMEL contribution number 4622.

Author contributions

All authors contributed extensively to the work presented in this paper. P.K.Q. and T.S.B. designed and performed the experiments, analysed data and wrote the paper. D.J.C. and J.E.J. performed the experiments and analysed data. L.M.U. analysed data.

Additional information

Supplementary information is available in the online version of the paper. Reprints and permissions information is available online at www.nature.com/reprints. Publisher's note: Springer Nature remains neutral with regard to jurisdictional claims in published maps and institutional affiliations. Correspondence and requests for materials should be addressed to P.K.Q.

Competing financial interests

The authors declare no competing financial interests.

Methods

Experiments. RITS-93 sailed from Punta Arenas, Chile on 20 March 1993 and arrived in Seattle, Washington on 7 May 1993. RITS-94 sailed from Seattle, Washington on 20 November 1993 and arrived in Punta Arenas, Chile on 7 January 1994. ACE-1 Leg 1 sailed from Seattle, Washington on 12 October 1995 and arrived in Hobart, Australia on 9 November 1995. ACE-1 Leg 2 sailed from Hobart, Australia on 15 November 1995 and returned to Hobart on 13 December 1995. ICEALOT sailed from Woods Hole, Massachusetts on 19 March 2008 and arrived in Reykjavik, Iceland on 24 April 2008. WACS-2 sailed from Woods Hole, Massachusetts on 20 May 2014 and returned to Woods Hole on 5 June 2014. NAAMES-1 sailed from Woods Hole, Massachusetts on 6 November 2015 and returned to Woods Hole on 1 December 2015.

Aerosol inlet. Aerosol particles were sampled 18 m above the sea surface through a 5 m mast. The inlet on top of the mast was automatically rotated into the relative wind to maintain nominally isokinetic flow and minimize the loss of supermicrometer particles. Air entered the inlet through a 5-cm-diameter hole, passed through a 7° expansion cone, and then into the 20-cm-inner-diameter sampling mast. The flow through the mast was $1 \text{ m}^3 \text{ min}^{-1}$. The transmission efficiency of the inlet for particles with aerodynamic diameters less than $6.5 \mu\text{m}$ (the largest size tested) is greater than 95% (ref. 52). The RH varied between cruises on the basis of ambient temperature and temperature control capabilities. The RH for RITS-93 and RITS-94 was $46 \pm 10\%$ and $32 \pm 6.8\%$, respectively, with no active temperature control in place²⁹. The RH for ACE-1 was $35 \pm 6\%$ with ambient air used to set the mast temperature⁵³. During ICEALOT, WACS-2 and NAAMES-1, the bottom 1.5 m of the mast were heated to establish a stable reference sampling RH. The reference RH for ICEALOT was $22 \pm 4\%$ with an average heated temperature of $15 \pm 3.6^\circ\text{C}$ above the ambient temperature⁵⁴. The reference RH for WACS-2 was $53 \pm 2\%$ with an average heated temperature of $5.6 \pm 1.0^\circ\text{C}$ above the ambient temperature⁵⁵. The reference RHs for NAAMES-1 were $24 \pm 8.2\%$ and $46 \pm 11\%$ for the northern, colder regions and southern, warmer regions of the cruise track, respectively. Associated heating of the sample air was $15 \pm 4.1^\circ\text{C}$ and $10 \pm 3.4^\circ\text{C}$, respectively.

Stainless-steel tubes extending into the heated portion of the mast were connected to downstream aerosol instrumentation. Conductive silicon tubing was used for making the connection to all samplers and instrumentation except for those that involved analysis of organic carbon, where stainless-steel tubing was used.

Aerosol chemical composition. Multi-jet cascade impactors⁵⁶, with 50% aerodynamic cutoff diameters of 0.18, 1.0 and $10 \mu\text{m}$, were used to collect size-segregated aerosol particles for quantification of inorganic ions and organic and elemental carbon. The time period of impactor sampling ranged from a few hours up to 48 h. To prevent contamination of the impactor substrates from the ship's stack, air flow to the impactors was controlled so that sampling took place only when the relative wind speed was greater than 3 m s^{-1} , the relative wind direction was forward of the beam, and particle number concentrations indicated that the sample air was free of ship emissions. Concentrations of Na^+ and SO_4^{2-} were determined with ion chromatography⁵³. Sea salt concentrations were calculated from

$$\text{Sea salt } (\mu\text{g m}^{-3}) = \text{Cl}^- (\mu\text{g m}^{-3}) + \text{Na}^+ (\mu\text{g m}^{-3}) \times 1.47 \quad (1)$$

where 1.47 is the seawater ratio of $(\text{Na}^+ + \text{K}^+ + \text{Mg}^{2+} + \text{Ca}^{2+} + \text{SO}_4^{2-} + \text{HCO}_3^-)/\text{Na}^+$ (ref. 57). Sea salt SO_4^{2-} concentrations were calculated from measured Na^+ concentrations and the mass ratio of sulfate to sodium in seawater of 0.252 (ref. 57). Concentrations of non-sea-salt (nss) SO_4^{2-} were calculated from the difference between the total and sea salt sulfate components.

Pre-combusted quartz fibre filters were used to collect samples for the quantification of organic carbon (OC) concentrations. Charcoal diffusion denuders were deployed upstream of the impactors to remove gas-phase organic species. OC concentrations were determined with a Sunset Laboratory thermal/optical analyser. Three temperature steps were used to evolve OC under O_2 -free conditions. The first step heated the filter to 230°C . The filter was then sequentially heated to 600°C and then 870°C . After cooling the sample down to 550°C , a He/O_2 mixture was introduced and the sample was heated in four temperature steps to 910°C to drive off elemental carbon. The transmission of light through the filter was measured to correct the observed elemental carbon for any OC that charred during the initial stages of heating. All aerosol OC concentrations are reported as micrograms of C. To account for the molecular weight of the non-carbon fraction of organic compounds, OC mass concentrations were converted to total particulate organic matter (POM) using a factor of 1.6 (ref. 58). For cruises where OC mass concentration data were not available (RITS-93, RITS-94, and ACE-1 Legs 1 and 2), POM mass fractions were based on average values from ICEALOT, WACS-2 and NAAMES-1 for each mode (Supplementary Figs 4–6).

Particle number size distributions. During RITS-93, RITS-94 and ACE-1 Legs 1 and 2, the number size distribution between 0.02 and $0.6 \mu\text{m}$ was measured every 10 min with a single differential mobility particle size (DMPS)²⁹. During ICEALOT, WACS-2 and NAAMES-1, the number size distribution between 0.02 and $0.8 \mu\text{m}$ was measured with two parallel DMPSs (University of Vienna⁵⁹) at the sampling humidity detailed above. Each DMPS was coupled to a condensation particle counter (CPC model 3760A, TSI). The ICEALOT, WACS-2 and NAAMES-1 size distributions consisted of 95 size bins due to the use of two DMPSs. The RITS and ACE size distributions consisted of 34 and 50 size bins, respectively. Mobility distributions were inverted to a number distribution assuming that a Fuchs–Boltzmann charge distribution resulted from the charge neutralizer used for each cruise (Kr^{85} for RITS-93, RITS-94, ACE-1 and Po^{210} for WACS-2 and NAAMES-1). Further details of the mobility distribution measurements and inversion methods are given in refs. 60,61. The number distribution between 0.9 to $10 \mu\text{m}$ was measured with an aerodynamic particle sizer (APS model 3321, TSI) at the sampling humidity detailed above. Aerodynamic diameters were converted to geometric diameters by dividing by the square root of the particle density. Densities were calculated from the measured chemical composition³. The DMPS and APS size distributions were then merged. The data were corrected for diffusional losses and size-dependent counting efficiencies. The estimated uncertainty in the number concentration in each size bin is $\pm 10\%$.

Measured CCN concentrations. A Droplet Measurement Technologies (DMT) CCN Counter (CCNC) was used to determine CCN concentrations of sub- $1.0 \mu\text{m}$ aerosol during ICEALOT at supersaturations ranging from 0.2 to 0.5%. A multi-jet cascade impactor with a 50% aerodynamic cutoff diameter of $1.0 \mu\text{m}$ was upstream of the CCNC at the sampling RH detailed above. The sample air was dried prior to reaching the CCNC. The CCNC was calibrated before and after the experiments using methods detailed in ref. 62. The uncertainty associated with the CCN number concentrations is estimated to be less than 10% and, for the conditions used here, less than 10% for the instrumental supersaturation^{62,63}.

Additional measurements. Radon was measured with a dual-flow-loop two-filter radon detector⁶⁴. The aerosol absorption coefficient was measured at 550 nm by monitoring the change in transmission through a filter with a particulate soot absorption photometer.

Lognormal-mode-fitting procedure. The merged DMPS-APS MBL number size distributions were averaged over the periods along the cruise track when impactor samples were collected for analysis of inorganic ions and organic carbon. These size distributions were fitted with multiple lognormal modes using the lognormal fit function in IGOR Pro (Wavemetrics).

The first mode to be fitted was in the largest diameter region of the size distribution. The mean diameter of the mode varied between experiments (0.17 to $0.45 \mu\text{m}$), due to different sampling humidities that affected water uptake and, therefore, particle size and differences in sizing instrumentation (see above). Because of this variability in mean diameter, no constraints were placed on the fitted parameters of the SSA mode as was done in ref. 21. The geometric standard deviation ranged from 2.2 to 2.7 across experiments. Two additional modes were then fitted—an accumulation mode with a mean diameter ranging from 0.10 to $0.23 \mu\text{m}$ and an Aitken mode with a mean diameter ranging from 0.02 to $0.08 \mu\text{m}$. The geometric standard deviation for both modes ranged from 1.3 to 1.75, narrower than that of the first fitted mode. The ability of the multi-modal fit to reproduce the measured size distribution was assessed with a chi-squared test. Only cases where the chi-squared value was less than the critical value at a significance level of 0.05 were included in the analysis.

Fitted volume size distributions were derived from the fitted number size distributions. Integrated number and volume concentrations in each of the three modes were calculated for comparison with measured sub- 0.18 , sub- 1 and sub- $10 \mu\text{m}$ Na^+ , nss SO_4^{2-} and OC mass concentrations. Aitken-mode number and volume concentrations were compared to sub- $0.18 \mu\text{m}$ Na^+ , nss SO_4^{2-} and OC. Accumulation-mode number and volume concentrations were compared to sub- 1 minus sub- $0.18 \mu\text{m}$ Na^+ , nss SO_4^{2-} and OC. SSA-mode number and volume concentrations were compared to sub- $10 \mu\text{m}$ Na^+ , nss SO_4^{2-} and OC.

Correlation analyses. All of the correlations that are presented are based on linear regressions. The goodness of the fit is expressed as the coefficient of determination, r^2 . Slope values are reported at the 95% confidence level.

Modelled CCN modal concentrations. Modal number size distributions and chemical composition were used to calculate modal CCN concentrations at supersaturations ranging from 0.1 to 1.0% as follows. Two extremes of chemical composition were used to calculate the range of potential CCN number concentrations for each mode. In the first case, each mode was assumed to be completely water soluble with the Aitken and accumulation modes composed of nss SO_4^{2-} (as NH_4HSO_4) and the SSA mode composed of inorganic sea salt. In the

second case, the measured chemical composition of Na^+ , nss SO_4^{2-} and OC from the impactor samples was used to determine the mass fraction of POM, POM_{MF} in each mode. For cruises where OC mass concentration data were not available (RITS-93, RITS-94, and ACE-1 Legs 1 and 2), POM mass fractions were based on average values from ICEALOT, WACS-2 and NAAMES-1 for each mode (Supplementary Figs 4–6). OC mass concentrations were converted to total POM using a factor⁵⁸ of 1.6 as follows

$$\text{POM} = \text{OC} (\mu\text{g C m}^{-3}) \times 1.6 \quad (2)$$

$$\text{POM}_{\text{MF}} = \text{POM} (\mu\text{g m}^{-3}) / (\text{POM} (\mu\text{g m}^{-3}) + \text{NH}_4\text{HSO}_4 (\mu\text{g m}^{-3}) + \text{sea salt} (\mu\text{g m}^{-3})) \quad (3)$$

where the sea salt concentration was determined from (1).

The Aitken-mode POM_{MF} was based on sub-0.18 μm impactor stage measurements. The accumulation-mode POM_{MF} was based on sub-1.0 μm minus sub-0.18 μm concentrations from the impactor measurements. The SSA-mode POM_{MF} was based on sub-10 μm concentrations from the impactor measurements. The sea salt, NH_4HSO_4 and POM mass fractions used in the calculations are shown in Supplementary Figs 4–6 for the Aitken, accumulation and SSA modes, respectively. Absolute concentrations are given in Supplementary Table 4. The POM fraction was assumed to be water insoluble. For a given composition and supersaturation, the critical diameter, D_c , for each mode was calculated from

$$D_c = (2 \times S_c^{2/3}) / (4A^3 / 27B)^{2/3} \quad (4)$$

where S_c is the critical supersaturation,

$$A = 2\sigma_s / (\rho_{\text{H}_2\text{O}}RT) \quad (5)$$

where σ_s is the surface tension of the solution/air interface and set at 72.8 dynes cm^{-1} , $\rho_{\text{H}_2\text{O}}$ is the density of water, R is the universal gas constant, and T is temperature, and

$$B = (n_i(1 - F_i)\rho_s M_{\text{H}_2\text{O}}) / (\rho_{\text{H}_2\text{O}}M_s) \quad (6)$$

where n_i is the number of ions in the solute, F_i is the organic insoluble fraction based on equation (3), ρ_s is the density of the solute, $M_{\text{H}_2\text{O}}$ is the molecular weight of water, and M_s is the molecular weight of the solute. Calculations for the Aitken and accumulation mode used ρ_s and M_s for NH_4HSO_4 . Calculations for the SSA mode used ρ_s and M_s for NaCl. Modal CCN concentrations were derived by summing the number of all particles in the fitted mode with diameters greater than D_c .

Comparison of measured and fitted mass concentrations. Fitted volumes for the Aitken, accumulation and SSA modes were converted to mass using densities derived from measured size-segregated chemical composition⁵³ for the ICEALOT cruise. For the density calculations, the Aitken and accumulation modes were assumed to be composed of nss SO_4^{2-} (as NH_4HSO_4) and POM based on measured concentrations of the sub-0.18 μm and sub-1 μm minus sub-0.18 μm impactor stages, respectively. The SSA mode was assumed to be composed of sea salt and POM on the basis of measured concentrations of the sub-10 μm impactor stages. Water mass was not included in the modal mass since the sampling RH during ICEALOT was <0.22%. The fitted modal masses are plotted on the x axis as ‘mass (from lognormal fit)’ in Supplementary Fig. 3. Measured mass concentrations for comparison to the Aitken and accumulation modal masses are the sum of the nss SO_4^{2-} (as NH_4HSO_4) and POM measured on the sub-0.18 μm and sub-1 μm minus sub-0.18 μm impactor stages, respectively. Measured mass concentrations for comparison to the SSA modal mass are the sum of the sea salt and POM mass concentrations measured on the sum of the sub-10 μm impactor stages. Measured mass concentrations are plotted on the y axis of Supplementary Fig. 3. Coefficients of determination, r^2 , for the comparison of the modelled and measured mass for the accumulation and SSA mode were 0.78 and 0.82. These high values indicate that the impactor stages used to make assumptions about the composition of the accumulation and SSA modes were able to explain 80% of the variance in these modes.

For the Aitken mode, r^2 was 0.23, indicating that the sub-0.18 μm impactor stage could explain only 20% of the variance in the Aitken-mode mass. In addition, the slope from the correlation was 18, indicating that the calculated Aitken-mode mass was much less than the mass on the sub-0.18 μm impactor stage. As shown in Fig. 2b, appreciable mass from the accumulation and coarse modes can tail into the sub-0.18 μm size range, which would account for this difference. The lack of correlation between measured and modelled mass for the Aitken mode helps to explain the weak correlation coefficients reported in Supplementary Table 3 and the difficulty in identifying the composition of the mode.

Comparison of measured and modelled CCN concentrations. The accuracy of modelled CCN concentrations was assessed by comparing the sum of CCN calculated to be in the Aitken, accumulation and SSA modes with CCN concentrations measured with a continuous-flow CCN counter (DMT) during ICEALOT, which had the most complete CCN data set. Including insoluble POM improved the agreement between measured and modelled values so that the difference was near zero for supersaturations ranging from 0.3 to 0.5% (Supplementary Fig. 8). At 0.2% supersaturation, the model underestimated the total CCN concentration by $20 \pm 10\%$. This difference could be due to instrumental uncertainties and/or the sensitivity of the calculated CCN concentrations to composition at lower supersaturations⁶⁵.

Data availability. The authors declare that all data supporting the findings of this study are available within the article and its supplementary information file. In addition, all underlying data are available at <https://saga.pmel.noaa.gov/data>.

References

- Bates, T. S., Coffman, D. J., Covert, D. S. & Quinn, P. K. Regional marine boundary layer aerosol size distributions in the Indian, Atlantic and Pacific Oceans: a comparison of INDOEX measurements with ACE-1 and ACE-2, and Aerosols99. *J. Geophys. Res.* **107**, 8026 (2002).
- Quinn, P. K. *et al.* Aerosol optical properties in the marine boundary layer during the first Aerosol Characterization Experiment (ACE-1) and the underlying chemical and physical aerosol properties. *J. Geophys. Res.* **103**, 16547–16563 (1998).
- Russell, L. M. *et al.* Carbohydrate-like composition of submicron atmospheric particles and their production from ocean bubble bursting. *Proc. Natl Acad. Sci. USA* **107**, 6652–6657 (2010).
- Quinn, P. K. *et al.* Contribution of sea surface carbon pool to organic matter enrichment in sea spray aerosol. *Nat. Geosci.* **7**, 228–232 (2014).
- Berner, A. *et al.* The size distribution of the urban aerosol in Vienna. *Sci. Tot. Environ.* **13**, 245–261 (1979).
- Holland, J. D. *The Chemistry of the Atmosphere and Oceans* (John Wiley, 1978).
- Turpin, B. J. & Lim, H.-J. Species contributions to PM_{2.5} mass concentrations: revisiting common assumptions for estimating organic mass. *Aerosol Sci. Tech.* **35**, 602–610 (2001).
- Winklmeyer, W., Reischl, G. P., Lindner, A. O. & Berner, A. New electromobility spectrometer for the measurement of aerosol size distributions in the size range 1 to 1000 nm. *J. Aerosol Sci.* **22**, 289–296 (1991).
- Bates, T. S. *et al.* Marine boundary layer dust and pollution transport associated with the passage of a frontal system over eastern Asia. *J. Geophys. Res.* **109**, D19S19 (2004).
- Stratmann, F. & Wiedensohler, A. A new data inversion algorithm for DMPS measurements. *J. Aerosol Sci.* **27**, 339–340 (1997).
- Lance, S., Medina, J., Smith, J. N. & Nenes, A. Mapping the operation of the DMT continuous flow CCN counter. *Aerosol Sci. Tech.* **40**, 242–254 (2006).
- Roberts, G. & Nenes, A. A continuous-flow streamwise thermal gradient CCN chamber for atmospheric measurements. *Aerosol Sci. Tech.* **39**, 206–221 (2005).
- Whittlstone, S. & Zahorowski, W. Baseline radon detectors for shipboard use: development and deployment in the First Aerosol Characterization Experiment (ACE-1). *J. Geophys. Res.* **103**, 16743–16751 (1998).
- Rose, D. *et al.* Calibration and measurement uncertainties of a continuous-flow cloud condensation nuclei counter (DMT-CCNC): CCN activation of ammonium sulfate and sodium chloride aerosol particles in theory and experiment. *Atmos. Chem. Phys.* **8**, 1153–1179 (2008).